ELSEVIER

Journal of Hazardous Materials A99 (2003) 111–144

Journal of Hazardous Materials

www.elsevier.com/locate/jhazmat

DISPLAY-2: a two-dimensional shallow layer model for dense gas dispersion including complex features

A.G. Venetsanos [a,b,*], J.G. Bartzis [a,c], J. Würtz [d], D.D. Papailiou [b]

[a] *National Center for Scientific Research "Demokritos", Environmental Research Laboratory, Institute of Nuclear Technology and Radiation Protection, 15310 Aghia Paraskevi, Attiki, Greece*

[b] *Laboratory of Technical Thermodynamics, Mechanical Engineering Department, University of Patras, Patra, Greece*

[c] *Department of Energy and Resources Management Engineering, Aristotle University of Thessaloniki, Kozani, Greece*

[d] *European Commission Joint Research Center ISPRA, Institute for Environment and Sustainability, Inland and Marine Water Unit, Ispra (Va), Italy*

Received 9 January 2003; received in revised form 9 January 2003; accepted 10 January 2003

Abstract

A two-dimensional shallow layer model has been developed to predict dense gas dispersion, under realistic conditions, including complex features such as two-phase releases, obstacles and inclined ground.

The model attempts to predict the time and space evolution of the cloud formed after a release of a two-phase pollutant into the atmosphere. The air-pollutant mixture is assumed ideal. The cloud evolution is described mathematically through the Cartesian, two-dimensional, shallow layer conservation equations for mixture mass, mixture momentum in two horizontal directions, total pollutant mass fraction (vapor and liquid) and mixture internal energy. Liquid mass fraction is obtained assuming phase equilibrium. Account is taken in the conservation equations for liquid slip and eventual liquid rainout through the ground. Entrainment of ambient air is modeled via an entrainment velocity model, which takes into account the effects of ground friction, ground heat transfer and relative motion between cloud and surrounding atmosphere. The model additionally accounts for thin obstacles effects in three ways. First a stepwise description of the obstacle is generated, following the grid cell faces, taking into account the corresponding area blockage. Then obstacle drag on the passing cloud is modeled by adding flow resistance terms in the momentum equations. Finally the effect of extra vorticity generation and entrainment enhancement behind obstacles is modeled by adding locally into the entrainment formula without obstacles, a characteristic velocity scale defined from the obstacle pressure drop and the local cloud height.

* Corresponding author.

E-mail address: venets@avra.ipta.demokritos.gr (A.G. Venetsanos).

0304-3894/03/$ – see front matter
doi:10.1016/S0304-3894(03)00011-6

The present model predictions have been compared against theoretical results for constant volume and constant flux gravity currents. It was found that deviations of the predicted cloud footprint area change with time from the theoretical were acceptably small, if one models the frictional forces between cloud and ambient air, neglecting the *Richardson* dependence.

The present model has also been validated in widely different experimental conditions such as the Thorney Island instantaneous isothermal releases 8 (unobstructed) and 21 (with semicircular fence), the EEC-55 two-phase propane experiment (with and without linear fence), the Desert Tortoise 4 two-phase ammonia experiment and the Hamburg DAT-638 instantaneous inclined plate experiment and the model predictions were found in reasonable agreement with the experimental data.

Keywords: Dense gas dispersion; Shallow layer; Two-phase releases; Entrainment; Thin obstacles; Liquid rainout

1. Introduction

The development of numerical tools to predict dense gas dispersion in the atmosphere is important for estimating the consequences of dense gas releases to the environment. These tools have to be able to take into account the complex conditions that exist in reality, like two-phase flow, obstacles and irregular terrain, in order to give realistic results to the decision makers.

Complex effects can be effectively accounted, through the use of CFD modeling (e.g. [1,2]) this approach however would require relatively large computational times.

Searching for a faster approach one option would be to apply a box model (see [3] for a list on box models) or a one-dimensional shallow layer model [4–6]. This is of course relatively fast, but has limitations. It cannot, for example, handle a two-dimensional obstacle or jets not aligned with the main wind.

In order to include two-dimensional effects and keep the computational times low enough one might select two-dimensional shallow layer modeling. Such idea has already been applied by Ott and Nielsen [7] in the SLAM model, by Hankin and Britter [8–10] in the TWODEE model and by Webber et al. [11], in the SHALLOW model, but on the other hand these models do not include any thermal effects nor interaction with obstacles.

One of the problems encountered in shallow layer modeling is the treatment of front propagation. The hydrostatic approximation is not valid at the front and experimental evidence indicates that the front Froude number is of the order of one (e.g. [12]).

To enforce a constant front Froude number, coupled with a hydrostatic shallow layer model, one may treat the front as a discontinuity and calculate its velocity based on the square root of the pressure head, as in a simple one-dimensional box model. A first difficulty with this approach is that one must keep track of the front footprint, a task which in case of a two-dimensional model may become very complicated. The main difficulty with this approach though is that even small unbalance introduces traveling waves in the following flow (e.g. [11]).

An alternative approach in obtaining a constant front Froude number is to enhance the shallow layer flow equations with special terms, which become active near the fronts (e.g. [8]). The implementation of this approach into the present model, but also into the

Nomenclature

A	area (m^2)
c_P	specific heat under constant pressure ($J\,kg^{-1}\,K^{-1}$)
C_f	friction factor
e	internal energy ($J\,kg^{-1}$)
h	cloud height (m)
H	heat flux ($J\,m^{-2}\,s^{-1}$)
n	normal vector
P	pressure (Pa)
q	contaminant liquid plus vapor mass fraction in the mixture
T	temperature (K)
T_*	temperature turbulence scale ($H_b/\rho c_P U_*$) (K)
u_i	cloud velocity in the i-direction ($m\,s^{-1}$)
U	velocity magnitude ($(u^2+v^2)^{1/2}$) ($m\,s^{-1}$)
U_{en}	entrainment velocity at top of cloud normal to the cloud surface ($m\,s^{-1}$)
U_*	friction velocity ($(\tau_b/\rho)^{1/2}$) ($m\,s^{-1}$)
$\vec{U}$	two-dimensional velocity vector (u, v)
w_{ld}	liquid phase deposition velocity ($m\,s^{-1}$)
x_i	Cartesian coordinate in the i-direction (m)
Δx	grid step in the x-direction (m)
Δy	grid step in the y-direction (m)
z	vertical coordinate (m)
z_0	roughness length (m)

Greek letters

α	cloud porosity, due to obstacles
Φ	stability function
κ	Von Karman constant (0.4)
ρ	density ($kg\,m^{-1}$)
$\Delta\rho$	$\rho - \rho_a$ ($kg\,m^{-1}$)
σ	turbulent Prandtl number
ς	obstacle resistance coefficient

Subscripts

a	ambient air
b	cloud bottom (coincides with ground)
e	entrainment
F	friction
h	heat
i	i-direction
κ	jet surface number
l	pollutant liquid phase
m	momentum

n	normal direction
o	obstacle
S	saturation
t	cloud top
v	pollutant vapor phase

one-dimensional model of Würtz [5], revealed waves in the following flow, although numerical problems of such kind were not reported by Hankin and Britter.

Attempts to use a fully hydrostatic model that does not enforce a constant front Froude number, have been made by Würtz et al. [4,5], and Meroney [6], with results generally in acceptable agreement with the experiments considered. This approach is expected to produce an accelerating cloud during the initial gravity slumping phase, because of not accounting for the pressure forces from the ambient air to the cloud. The cloud spreading will eventually be overestimated. The degree of overestimation will depend upon the particular modeling of the frictional forces between cloud and ground of the frictional forces between cloud and ambient air and of the entrainment of ambient air.

The present contribution describes in detail the two-dimensional, shallow layer model DISPLAY-2. This is a hydrostatic model with no account of the pressure forces acted from ambient air to the cloud. The model accounts for two-phase releases, inclined ground and obstacles. Validation results are presented for the Thorney Island experiments 8 and 21, the EEC-55 propane experiment, the Desert Tortoise 4 ammonia experiment and the Hamburg DAT-638 inclined plate experiment.

2. Mathematical formulation

2.1. Definitions–assumptions

The present model layer-averaged conservation equations were derived by averaging the three-dimensional, time dependent Reynolds averaged conservation equations, including liquid slip terms [13], vertically over the cloud height.

The layer-averaged value of a given variable is given by

$$\bar{\varphi} = \frac{1}{h}\int_{z_b}^{z_t} \varphi \, \mathrm{d}z \tag{2.1}$$

where h is the cloud height, which is the difference between the top and bottom surfaces of the cloud:

$$h(x, y, t) = z_t(x, y, t) - z_b(x, y) \tag{2.2}$$

In deriving the model conservation equations it was assumed that the layer average of products of variables is approximately equal to the product of the individual layer-averaged variables, multiplied by some constant.

$$\overline{\varphi_1\varphi_2} \approx C\overline{\varphi_1\varphi_2} \tag{2.3}$$

For simplicity reasons it was assumed that the constant of proportionality is one in all cases. This assumption would be exact if the distribution of all the variables involved in the product is constant within the layer considered.

For the momentum equations, the hydrostatic pressure approximation was assumed valid for the entire cloud (except close to obstacles). No special terms were added to the momentum equations to account for the pressure forces acted from the ambient air to the cloud. Additionally the cloud front velocities were not set to get a constant front Froude number.

In deriving the model equations, horizontal gradients of horizontal turbulent fluxes were neglected, assumed being much lower to the vertical gradients.

Entrainment of ambient air was modeled as a transport mechanism through the cloud top surface, with the entrainment velocity defined by

$$\frac{U_{\mathrm{en}}}{n_z} \equiv \frac{\partial h}{\partial t} + u_{\mathrm{t}}\frac{\partial h}{\partial x} + v_{\mathrm{t}}\frac{\partial h}{\partial y} - w_{\mathrm{t}} \tag{2.4}$$

where n_z is the vertical component of the top surface normal vector. At the cloud top the conditions were assumed to be that of the ambient flow at the same height.

In general as a first step approach, top hat profiles were assumed for concentration and density. Hankin and Britter [10] reported best overall agreement of predicted versus observed maximum concentrations of the Thorney Island 8 experiment, using exponential profiles. They tested top hat, Gaussian and exponential profiles, using the same entrainment formulation. On the other hand, formula (2.4) shows that entrainment velocity is directly linked to the cloud height definition, so changing type of profile would imply modification of the constants in the entrainment model (see also the discussion on entrainment model calibration in Section 2.6).

Finally, as for the cloud composition, it was assumed to be an ideal mixture of the pollutant with air. The pollutant can be under two-phase conditions (liquid and vapor). The mixture was assumed to be in thermodynamic equilibrium, i.e. all components sharing the same temperature and pressure. The component physical properties were assumed to be in general functions of temperature and pressure.

2.2. Conservation equations

The definitions and assumptions introduced above, in addition to more assumptions to be discussed later, led us to the following system of two-dimensional layer-averaged conservation equations.

Mixture mass

$$\frac{\partial \bar{\rho} h}{\partial t} + \frac{\partial \bar{\rho} h \bar{u}_j}{\partial x_j} = \frac{\rho_{\mathrm{at}} U_{\mathrm{en}}}{n_z} - \bar{\rho}\bar{q}_{\mathrm{l}}\bar{w}_{\mathrm{ld}} + \sum_{\kappa}\left[\frac{\rho_\kappa A_\kappa U_{\mathrm{n}\kappa}}{\Delta x\,\Delta y}\right] \tag{2.5}$$

Total pollutant mass

$$\frac{\partial \bar{\rho} h \bar{q}}{\partial t} + \frac{\partial \bar{\rho} h \bar{q} \bar{u}_j}{\partial x_j} = -\bar{\rho}\bar{q}_{\mathrm{l}}\bar{w}_{\mathrm{ld}} + \sum_{\kappa}\left[\frac{\rho_\kappa A_\kappa U_{\mathrm{n}\kappa} q_\kappa}{\Delta x\,\Delta y}\right] \tag{2.6}$$

Mixture momentum in x, y horizontal directions

$$\frac{\partial \bar{\rho} h \bar{u}_i}{\partial t} + \frac{\partial \bar{\rho} h \bar{u}_j \bar{u}_i}{\partial x_j} = \frac{\rho_{\mathrm{at}} U_{\mathrm{en}} u_{i\mathrm{at}}}{n_z} + \sum_{\kappa} \left[\frac{\rho_\kappa A_\kappa U_{\mathrm{n}\kappa} u_{i\kappa}}{\Delta x \, \Delta y} \right] - \left\{ \frac{1}{2} \frac{\partial \Delta \bar{\rho} g h^2}{\partial x_i} + \Delta \bar{\rho} g \frac{\partial z_{\mathrm{b}}}{\partial x_i} h \right\} - \frac{1}{2} \frac{\varsigma_i}{\Delta x_i} \bar{\rho} |\bar{u}_i| \bar{u}_i h - \frac{1}{2} \bar{\rho} C_{\mathrm{fb}} \bar{U} \bar{u}_i - \frac{1}{2} \rho_{\mathrm{a}} C_{\mathrm{ft}} \left| \bar{\vec{U}} - \vec{U}_{\mathrm{at}} \right| (\bar{u}_i - u_{i\mathrm{at}}) \tag{2.7}$$

Mixture internal energy

$$\frac{\partial \bar{\rho} h \bar{e}}{\partial t} + \frac{\partial \bar{\rho} h \bar{e} \bar{u}_j}{\partial x_j} = \frac{\rho_{\mathrm{at}} U_{\mathrm{en}} e_{\mathrm{at}}}{n_z} + \sum_{\kappa} \left[\frac{\rho_\kappa A_\kappa U_{\mathrm{n}\kappa} e_\kappa}{\Delta x \, \Delta y} \right] + \bar{P} \left[- \frac{\partial h \bar{u}_j}{\partial x_j} - \frac{\partial h}{\partial t} + \frac{U_{\mathrm{en}}}{n_z} - \bar{q}_{\mathrm{l}} \bar{w}_{\mathrm{ld}} \frac{\bar{\rho}}{\bar{\rho}_{\mathrm{l}}} + \sum_{\kappa} \left[\frac{A_\kappa U_{\mathrm{n}\kappa}}{\Delta x \, \Delta y} \right] \right] - \bar{\rho} \bar{q}_{\mathrm{l}} \bar{w}_{\mathrm{ld}} \bar{e}_{\mathrm{l}} + \frac{1}{2} \bar{\rho} \bar{c}_P \frac{C_{\mathrm{fb}}}{\sigma} \bar{U} (T_{\mathrm{ab}} - \bar{T}) \tag{2.8}$$

In the above equations the layer-averaged mixture density is calculated from the layer-averaged component densities through the relation:

$$\frac{1}{\bar{\rho}} = \frac{\bar{T} \bar{R}}{\bar{P}} + \frac{\bar{q}_{\mathrm{l}}}{\bar{\rho}_{\mathrm{l}}}, \qquad \bar{R} = (1 - \bar{q}) R_{\mathrm{a}} + (\bar{q} - \bar{q}_{\mathrm{l}}) R_{\mathrm{v}} \tag{2.9}$$

where ideal gas equations of state are used for air and pollutant vapor, with R_{a} and R_{v} the respective gas constants.

The layer-averaged hydrostatic pressure is calculated from the relation:

$$\bar{P} = P_{\mathrm{t}} + \bar{\rho} g \frac{h}{2}, \qquad P_{\mathrm{t}} = P_{\mathrm{ref}} \exp \left(\frac{g(z_{\mathrm{ref}} - z_{\mathrm{t}})}{R_{\mathrm{a}} T_{\mathrm{a}}} \right) \tag{2.10}$$

where P_{ref} is the ambient pressure at elevation z_{ref} (much higher than cloud height) and T_{a} is the ambient air temperature, assumed constant.

The layer-averaged mixture internal energy was defined as function of the layer-averaged component internal energies, using the relation:

$$\bar{e}(\bar{T}, \bar{P}, \bar{q}, \bar{q}_{\mathrm{l}}) = (1 - \bar{q}) \bar{e}_{\mathrm{a}}(\bar{T}) + (\bar{q} - \bar{q}_{\mathrm{l}}) \bar{e}_{\mathrm{v}}(\bar{T}, \bar{P}) + \bar{q}_{\mathrm{l}} \bar{e}_{\mathrm{l}}(\bar{T}, \bar{P}) \tag{2.11}$$

A similar equation was used for connecting the layer-averaged mixture physical properties (except density) to the layer-averaged component properties, assuming that the component properties are known functions of temperature only.

Layer-averaged temperatures $\bar{T}$ were derived iteratively from the $\bar{e}$ definition equation, knowing the pressure, internal energy, mass fraction and liquid mass fraction.

The source terms under the summations over κ, represent the contributions from jets (in case of jet releases), where ρ_κ, A_κ, $U_{\mathrm{n}\kappa}$ and e_κ are the jet density, area, velocity and internal

energy, respectively. The jet density and internal energy were calculated as functions of the input data T_κ, P_κ and $q_{l\kappa}$, which are the jet temperature, pressure and liquid mass fraction, respectively.

2.3. Ambient flow conditions

The ambient air flow outside the cloud, was assumed to follow the Monin–Obukhov theory (see [14]), according to which velocity and temperature vertical profiles are given by

$$\frac{\kappa U_\mathrm{a}(z)}{U_{*\mathrm{a}}} = \Psi_\mathrm{m}(n_\mathrm{a}) = \int_{z_0}^{z+z_0} \frac{\Phi_\mathrm{m}(n_\mathrm{a})}{z}\,\mathrm{d}z \tag{2.12}$$

$$\frac{\kappa(T_\mathrm{ba} - T_\mathrm{a}(z))}{T_{*\mathrm{a}}} = \Psi_\mathrm{h}(n_\mathrm{a}) = \int_{z_0}^{z+z_0} \frac{\Phi_\mathrm{h}(n_\mathrm{a})}{z}\,\mathrm{d}z \tag{2.13}$$

where

$$n_\mathrm{a} = \frac{z}{L_\mathrm{MOa}} \quad \text{and} \quad L_\mathrm{MOa} = -\frac{\rho_\mathrm{a} c_{P\mathrm{a}} T_\mathrm{a} U_{*\mathrm{a}}^3}{\kappa g H_\mathrm{ba}} \tag{2.14}$$

The universal stability functions are calculated according to Venetsanos et al. [15] by

$$\Phi_\mathrm{m}(n) = \begin{cases} (1-15n)^{-1/4}, & n \le 0 \\ 1 + 4.7n, & n \ge 0 \end{cases} \tag{2.15}$$

$$\Phi_\mathrm{h}(n) = \begin{cases} 0.72(1-15n)^{-1/2}, & n \le 0 \\ 0.72 + 4.7n, & n \ge 0 \end{cases} \tag{2.16}$$

Using the above velocity and temperature vertical profiles, the cloud-averaged ambient velocity and temperature can be expressed as following:

$$\bar{U}_\mathrm{a} \equiv \frac{1}{h}\int_{z_0}^{z_0+h} U_\mathrm{a}(z)\,\mathrm{d}z = \left(1 + \frac{z_0}{h}\right) U_\mathrm{at} - \frac{U_{*\mathrm{a}}}{\kappa}\overline{\Phi_\mathrm{m}} \tag{2.17}$$

$$\bar{T}_\mathrm{a} \equiv \frac{1}{h}\int_{z_0}^{z_0+h} T_\mathrm{a}(z)\,\mathrm{d}z = \left(1 + \frac{z_0}{h}\right) T_\mathrm{at} + \frac{T_*}{\kappa}\overline{\Phi_\mathrm{h}} \tag{2.18}$$

The effect of obstacles on the above profiles was neglected. This effect can be accounted by running a three-dimensional, steady state prognostic or diagnostic model, prior to the shallow layer model. The three-dimensional solution would then be used to feed the shallow layer model with the appropriate ambient flow values at each point in space. This approach however would require large computational times and therefore limit the applicability of shallow layer models.

2.4. Ground friction and heat transfer

The shear stress at the ground is given by

$$\tau_\mathrm{b} = \tfrac{1}{2}\bar{\rho} C_\mathrm{fb} \bar{U}^2 \tag{2.19}$$

where the ground friction factor is defined as

$$C_{\mathrm{fb}} \equiv 2\left(\frac{U_*}{\bar{U}}\right)^2, \qquad U_* \equiv \left(\frac{\tau_{\mathrm{b}}}{\bar{\rho}}\right)^{1/2} \tag{2.20}$$

The ground heat flux is given by

$$H_{\mathrm{b}} = \frac{1}{2}\bar{\rho}\bar{c}_P \frac{C_{\mathrm{fb}}}{\sigma}\bar{U}(T_{\mathrm{b}} - \bar{T}) \tag{2.21}$$

where the turbulent Prandtl number is defined as

$$\sigma \equiv \frac{T_{\mathrm{b}} - \bar{T}}{T_*}\frac{U_*}{\bar{U}}, \qquad T_* \equiv \frac{H_{\mathrm{b}}}{\bar{\rho}\bar{c}_P U_*} \tag{2.22}$$

The ground friction factor and turbulent Prandtl number were calculated by applying the Monin–Obukhov theory again inside the cloud. The velocity and temperature profiles used outside the cloud are also applied here, replacing the ambient with local cloud properties:

$$\frac{\kappa U(z)}{U_*} = \Psi_{\mathrm{m}}(n) = \int_{z_0}^{z+z_0} \frac{\Phi_{\mathrm{m}}(n)}{z}\,\mathrm{d}z \tag{2.23}$$

$$\frac{\kappa(T_{\mathrm{b}} - T(z))}{T_*} = \Psi_{\mathrm{h}}(n) = \int_{z_0}^{z+z_0} \frac{\Phi_{\mathrm{h}}(n)}{z}\,\mathrm{d}z \tag{2.24}$$

where

$$n = \frac{z}{L_{\mathrm{MO}}} \quad \text{and} \quad L_{\mathrm{MO}} = -\frac{\rho c_P T U_*^3}{\kappa g H_{\mathrm{b}}} \tag{2.25}$$

Using the above vertical profiles, the cloud-averaged velocity and temperature become

$$\bar{U} = U_{\mathrm{t}} - \frac{U_*}{\kappa}\overline{\Phi_{\mathrm{m}}} \quad \text{and} \quad \bar{T} = T_{\mathrm{t}} + \frac{T_*}{\kappa}\overline{\Phi_{\mathrm{h}}} \tag{2.26}$$

with these relations the friction factor and turbulent Prandtl number can be expressed as following:

$$C_{\mathrm{fb}} = 2\left(\frac{\kappa}{\overline{\Psi_{\mathrm{m}}}}\right)^2 \tag{2.27}$$

$$\sigma = \frac{\overline{\Psi_{\mathrm{h}}}}{\overline{\Psi_{\mathrm{m}}}} \tag{2.28}$$

2.5. Cloud–ambient air friction

The friction between cloud and ambient air at the cloud top was modeled using the vector difference between average cloud velocity and velocity of the ambient flow at the cloud top.

$$\tau_{\mathrm{t}} = \tfrac{1}{2}\rho_{\mathrm{a}} C_{\mathrm{ft}}(\vec{\bar{U}} - \vec{U}_{\mathrm{at}})^2 \tag{2.29}$$

The friction factor at the cloud top C_{ft} is estimated with reference to the limiting conditions of passive dispersion in a constant stress layer, by requiring that under these conditions the friction at the cloud top and the friction on the ground counteract and balance each other.

$$\tfrac{1}{2}\rho_a C_{ft}(\bar{U} - U_{at})^2 = \rho_a U_*^2 \tag{2.30}$$

from which, with the aid of relation (2.26), we get

$$\rho_a U_*^2 \left\{ \left(\frac{\overline{\Phi_m}}{\kappa} \right)^2 \frac{C_{ft}}{2} \right\} = \rho_a U_*^2 \tag{2.31}$$

from which it follows that

$$C_{ft} = 2\left(\frac{\kappa}{\overline{\Phi_m}} \right)^2 \tag{2.32}$$

In the present model the top friction factor becomes 0.32 for neutral conditions. This is fairly large compared to values in the range 0.001–0.01 usually encountered for C_{fb}. High values of top friction factors have been used also by other investigators, e.g. Carpenter et al. [16] used a value of 0.6, while Ott and Nielsen [7] used a ratio of top to bottom friction, which in the absence of ambient wind becomes $(\rho_a/\rho)(\ln(h/z_0) - 1)$.

Wheatley and Prince [17], on the other hand, modeled the frictional forces at the cloud top, by defining a top friction factor depending on the bulk Richardson number:

$$C_{ft} = 2\frac{0.001}{Ri_b}, \qquad Ri_b = \frac{g\,\Delta\bar{\rho}h}{\rho_a \bar{u}^2} \tag{2.33}$$

Such an approach would produce very small top friction for large values of the Richardson number.

The way the cloud top frictional forces are modeled affects the cloud dispersion during the initial phases of gravity slumping. Webber and Brighton [18] briefly examined the effect of the frictional forces, during the gravity slumping phase of a cylindrical cloud without wind. In the present model, as will be shown later, the high value of the top friction factor results in restricting the tendency of the cloud to accelerate during the initial gravity slumping phase and thus limits the initial cloud spreading to acceptable levels.

2.6. Entrainment velocity model

One of the pioneering works in dense gas dispersion modeling, related to the present work, is that of Eidsvik [19]. Eidsvik developed a box model in which the vertical entrainment velocity was calculated from

$$w_e = \frac{a_1}{1 + a_2 Ri} a_3 U' \tag{2.34}$$

where Ri is the Richardson number defined using U'

$$Ri = \frac{gh\,\Delta\bar{\rho}}{\bar{\rho}U'^2} \tag{2.35}$$

and U' is the following characteristic turbulent velocity

$$U' = [U_*^2 + (a_4 U_H)^2]^{1/2}$$

which is a combination of the mechanical turbulence characteristic velocity U_* and the convective turbulent velocity scale

$$U_H = \left(\frac{H_b g h}{\bar{\rho}\bar{c}_P \bar{T}}\right)^{1/3} = \left(\frac{g c_F}{2\sigma}\bar{u}\frac{T_a - \bar{T}}{\bar{T}}h\right)^{1/3} \tag{2.37}$$

Eidsvik used the following constants:

$$a_1 = 0.3, \qquad a_1/a_2 = 3.5, \qquad a_3 = 1.3, \qquad a_4 = 0.54 \tag{2.38}$$

Coefficient a_1 was selected with reference to the entrainment law suggested by Tennekes and Lumley [20] for the approximate growth of a neutral boundary layer. Coefficient a_2 was chosen with reference to the Kato and Philips [21] entrainment law for strongly stratified shear flow. The remaining coefficients were calibrated. Coefficient a_3 accounts for the difference between entrainment in a passive scalar cloud (this model gives $0.39U_*$) and entrainment in a neutral boundary layer. Coefficient a_4 characterizes the relative contributions of convective and mechanical entrainment.

For the limiting case of a passive scalar cloud, it can be mentioned that an entrainment velocity coefficient close to 0.4 has been reported or can be deduced from other independent studies. Stretch [22] found entrainment velocity $0.41U_*$, assuming the following cloud height definition:

$$h(x, y, t) = \frac{\int_{z_b}^{\infty} \Delta\rho \, \mathrm{d}z}{\Delta\rho_b} \tag{2.39}$$

Nielsen [23] reported entrainment velocity approximately $0.75U_*$, using Sutton's [24] analytical solution, assuming the cloud height defined as two times the cloud centroid, but it can be shown that using Stretch's definition of cloud height, results in entrainment velocity approximately $0.43U_*$.

Würtz and others [4,5] found reasonably good agreement between experiments and predictions of the one-dimensional shallow layer model DISPLAY-1, using the following top entrainment model, which is an extension of Eidsvik's formulation:

$$w_e = a_1 a_3 c_F \left[\bar{U}^2 + \left(\frac{a_4}{c_F}U_H\right)^2 + \left(\frac{a_5}{c_F}\Delta\bar{U}\right)^2\right]^{1/2} \tag{2.40}$$

$$\bar{U}^2 = \bar{u}^2 + \bar{v}^2, \qquad \Delta\bar{U}^2 = (\bar{u} - \bar{u}_a)^2 + (\bar{v} - \bar{v}_a)^2, \qquad c_F^2 = \tfrac{1}{2}(C_{fb}) \tag{2.41}$$

$$a_2 = 0, \qquad a_1 a_3 c_F = 0.03, \qquad a_4 = 0.78, \qquad a_5 = c_F \tag{2.42}$$

In this model the U_* dependence was replaced with a dependence on the cloud velocity, using a value of $c_{fb} = 0.012$ for the ground friction factor. An extra velocity difference term was also added, to take into account of the entrainment produced, due to the relative motion between the cloud and the surrounding atmosphere. Finally the Richardson dependence was

dropped, because very small entrainment rates and corresponding large overestimations of concentrations were produced, when keeping this term.

In the present context we have used the Würtz entrainment formulation, because of its success in one-dimensional shallow layer modeling. The entrainment velocity normal to the cloud top surface U_{en} is calculated from relations (2.40) and (2.41), where the constants have been slightly modified, to get a better agreement between the two-dimensional shallow layer model and the experiments.

$$a_2 = 0, \qquad a_1 a_3 c_F = 0.035, \qquad a_4 = 0.82, \qquad a_5 = c_F \tag{2.43}$$

In the present model we have also dropped the Richardson dependence, because similarly to the one-dimensional model, large overestimation of concentrations were obtained for the Thorney Island 8 ground sensors, when keeping this dependence.

Finally, it should be mentioned that the present entrainment model calibration is related to the top hat profiles used in this study. If one uses linear profiles, instead of top hat profiles, then based on relation (2.4), the entrainment velocity will have to be increased by factor of 2 approximately, since the height is also increased by factor of 2.

2.7. Obstacle effects

Obstacles encountered by a dispersing cloud act either by completely blocking the cloud or by exerting a drag force on the passing cloud. In the second case extra vorticity is generated at the downwind side of the obstacle, which leads to enhancement of the entrainment (e.g. [25]).

From existing approaches to model the obstacle effects can be mentioned those of Cleaver et al. [26] for a box model, of Würtz [5] for a one-dimensional shallow layer model and of Andronopoulos et al. [1] for a CFD model.

Cleaver et al.'s approach, which consists of imposing an increase of the cloud width and height at the location of the obstacle, according to given laws, does not have the generality to be applied in a two-dimensional shallow layer model.

Würtz's approach consists of modeling the obstacle pressure drop in the flow direction, using a relation originally proposed by Idelchik [27] for the flow through orifices with sudden change in velocity and flow area and additionally adding an extra term equal to $0.71\bar{u}_{\mathrm{a}}$, to the entrainment velocity in the region of one obstacle height upwind of the obstacle (see Fig. 1), to account for entrainment enhancement upwind of the obstacle. It should be noted that the Würtz extra upwind entrainment was found to overestimate entrainment in the present two-dimensional shallow layer model. On the other hand, this extra term does not have enough generality, due to its dependence solely on the ambient velocity field.

Based on the previous studies of Würtz [5] and Andronopoulos et al. [1] we model obstacle pressure drop in the flow direction, using the relation proposed by Idelchik [27] for the flow through orifices with sudden change in velocity and flow area. Denoting with subscripts 1, 0 and 2 the conditions before, at and after the obstacle, respectively, the pressure drop in the i-direction is given by

$$\Delta P_{i12} = \tfrac{1}{2}\varsigma_{i0}\rho|\bar{u}_{i0}|\bar{u}_{i0} \tag{2.44}$$

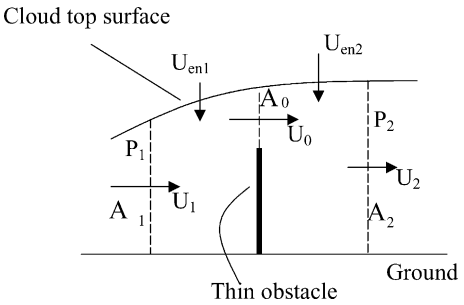

Fig. 1. Sketch of cloud in the vicinity of a thin obstacle.

$$\varsigma_{i0} = \left[\frac{\sqrt{2}}{2} \sqrt{1 - \frac{A_{i0}}{A_{i1}}} + \left(1 - \frac{A_{i0}}{A_{i2}}\right) \right]^2 \tag{2.45}$$

$$Re = \frac{u_{i0} D_{\mathrm{h}}}{v} > 10^5$$

where A_{i1}, A_{i0} and A_{i2} are the cloud vertical surfaces (ground to obstacle top) before at and after the obstacle, respectively (see Fig. 1). In this case the obstacle is not aligned with one of the axis, we generate a step description of it that fits exactly on the grid.

We additionally model the enhancement of the entrainment due to the extra vorticity generated downwind of the obstacle, by adding locally (at the obstacle downwind position 2) an obstacle characteristic velocity $U_{\mathrm{o}2}$ to the entrainment velocity without obstacles U_{en} (see Fig. 1).

$$U_{\mathrm{en}2} = U_{\mathrm{en}} + U_{\mathrm{o}2} \tag{2.46}$$

No extra entrainment is added upwind of the obstacle

$$U_{\mathrm{en}1} = U_{\mathrm{en}} \tag{2.47}$$

We furthermore assume that $U_{\mathrm{o}2}$ can be related to the pressure drop across the obstacle $\partial P/\partial x_i$. Then using dimensional analysis we may get

$$U_{\mathrm{o}2}^2 = f\left(h \frac{1}{\rho} \frac{\partial P}{\partial x_i}\right) = \frac{h}{\rho} \frac{\partial P}{\partial x_i} \approx \frac{h_0}{\rho} \frac{\Delta P_{i12}}{\Delta x_{i12}} \tag{2.48}$$

Finally, expressing the obstacle pressure drop in term of the obstacle resistance coefficient introduced earlier we get

$$U_{\mathrm{o}2}^2 = \frac{h_0}{2} \frac{\varsigma_{i0}}{\Delta x_{i12}} \bar{u}_{i0}^2 \tag{2.49}$$

2.8. Liquid phase calculation

Liquid phase appearance criterion and liquid mass fraction calculation is performed assuming phase equilibrium, based on Housiadas et al [13]. More specifically, liquid

phase appears when the pollutant mass fraction exceeds its saturated value in the mixture

$$q > q_S = \frac{P_S}{P_S + (P - P_S)R_v/R_a} \tag{2.50}$$

If such a condition is met, a saturation state is assumed to exist in the gaseous phase, from which the liquid mass fraction can be calculated:

$$\frac{q - q_l}{1 - q_l} = q_S \Leftrightarrow q_l = \frac{q - q_S}{1 - q_S} \tag{2.51}$$

2.9. Deposition velocity and liquid rainout

Liquid rainout through the ground is assumed to occur at the rate by which liquid falls to the ground $\rho q_l w_{ld}$, where w_{ld} is the vertical liquid deposition velocity.

Droplet fall velocity has been modeled in atmospheric precipitation predictions by Ogura and Takahashi [28] assuming spherical droplets, falling at their terminal falling speed [29], distributed in diameter, according to Marshall and Palmer distribution with droplet fall Reynolds number in the turbulent regime. This model generates large droplet falling speeds, which result in unrealistic two-dimensional shallow layer predictions in comparison to experimentally observed behavior, for two-phase near ground releases.

In the present context we claim that in case of two-phase near ground releases the falling droplets do not reach a terminal speed or a fully turbulent falling regime, because of the small distances from the ground. In such a situation we assume that the deposition velocity can be approximated as a fraction of the Ogura and Takahashi terminal speed, but corresponding to the laminar regime. Under these conditions it is shown in Appendix A that

$$w_{ld} = C_{ld}\left(\frac{\rho q_l}{\rho_l}\right)^{1/2} \tag{2.52}$$

In the present model we have estimated the constant to be: $C_{ld} \approx 5.0$.

3. The numerical approach

The discretization of the differential equations is made using the control volume formulation [30], on a terrain following grid. The control volumes for the velocities $\bar{u}$ and $\bar{v}$ are staggered in the x and y directions, respectively.

Convective terms are discretized using a monotone upstream-centered schemes for conservation laws (MUSCLE) type second order upwind scheme with MinMod limiters [31].

The differential equations are solved using the Gauss–Seidel iterative method. The time step is permitted to vary with time. The maximum time step is limited by requiring the Courant number not to exceed 0.5.

4. Comparison against theoretical results

4.1. Constant volume, axisymmetric gravity currents

Grundy and Rottman [32] presented a similarity solution of the shallow layer equations at large times, for planar and axisymmetric gravity currents, without entrainment (constant volume). The axisymmetric results will be used for comparison with the present model predictions.

If we assume a cylindrical cloud, of volume V, density ρ such that $\Delta\rho/\rho_a \ll 1$ and initial footprint area A_0, then the similarity solution gives a linear dependence of the gravity current footprint area A with time

$$\frac{A(t)}{A_0} = \left(\frac{(4\beta)^2}{(4-\beta^2)\pi}\right)^{1/2} \frac{t}{t_0} \quad \text{for} \quad t \gg t_0 \tag{4.1}$$

where $t_0 = (A_0/(Vg(\Delta\rho/\rho_a)))^{1/2}$ and β is the front Froude number, which was assumed constant.

The above constant front Froude number linear dependence was well reproduced by Hankin and Britter [8,9], by adding source terms in the two-dimensional layer-averaged momentum equations, to model the pressure forces acted by the ambient air to the cloud. For absent ambient wind and a front Froude number equal to one, the Hankin and Britter source terms take the form

$$S_u = -\frac{\rho_a}{2}\left(\frac{\partial h\bar{u}}{\partial t}\right) \quad \text{and} \quad S_v = -\frac{\rho_a}{2}\left(\frac{\partial h\bar{v}}{\partial t}\right) \tag{4.2}$$

The present model uses the hydrostatic assumption for the entire cloud (except close to obstacles), therefore it does not account for pressure forces from the ambient air to the cloud. It accounts though for the ambient air frictional forces at the cloud top, a factor that was assumed negligible in the model of Hankin and Britter, which can hold if the velocity gradient is nearly zero at the top.

The results obtained with the present approach are presented in Fig. 2. The case modeled was a cylinder of 10 m height, 5 m diameter and $\Delta\rho/\rho_a = 0.5$. The calculations were performed for the quarter of the cloud, for a constant grid step of 0.5 m in both x and y directions and a maximum Courant number equal to 0.5. It can be observed that the present model predicts a cloud, which initially accelerates and decelerates later on but whose footprint area does not deviate significantly from the theoretical linear dependence. The effect of the top friction term can be evaluated by comparing to the results that were obtained with the bottom friction terms only. It can be observed in Fig. 2 that the deviations from the linear dependence are unacceptably large if the top friction term is ignored.

4.2. Constant flux, axisymmetric gravity currents

The previous case was for a gravity current of constant volume. The case of volume increasing linearly with time was considered by Britter [33], who suggested the following

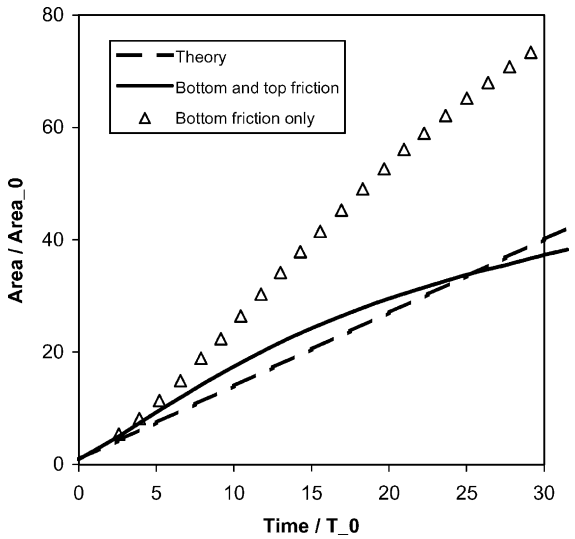

Fig. 2. Constant volume axisymmetric gravity current area history. Predictions with present model with bottom and top friction, predictions with present model neglecting top friction and theoretical curve of Grundy and Rottman [32].

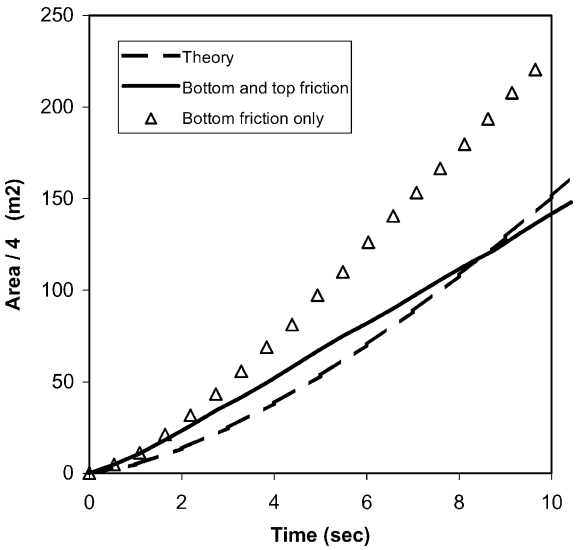

Fig. 3. Constant flux axisymmetric gravity current area history. Predictions with present model with bottom and top friction, predictions with present model neglecting top friction and theoretical curve of Britter [33].

relationship for the change with time of the cloud footprint area

$$A(t) = \frac{\pi}{0.75^{1.5}(2\pi)^{0.5}} \left(g \frac{\Delta\rho}{\rho_a} \dot{V} \right)^{0.5} t^{1.5} \tag{4.3}$$

The results of the present model for this case are shown in Fig. 3. The test case modeled was a vertical jet of 1 m^2 area, 20 m s^{-1} vertical velocity and $\Delta\rho/\rho_a = 0.5$. The calculations were performed for the quarter of the jet, on the same grid, as in the previous constant volume case. It can be observed in Fig. 3 that the present model predictions do not deviate significantly from the above theoretical relation, while in the case of no top friction the discrepancy is high.

5. Experimental validation

5.1. Experimental data

The experiments used for model validation covered a wide range of experimental conditions as shown in Table 1.

The Thorney Island experiments, McQuaid and Roebuck [34], were large scale instantaneous isothermal releases of freon 12/nitrogen mixture on flat ground with and without obstacles. They were organized by the Health and Safety Executive (UK). Trials 8 and 21 were chosen for simulation because they were fully successful. Trial 21 was chosen also because as reported the interaction of the cloud with the fence was strong due to the relatively low wind speed. During trials 8 and 21 volume concentrations were measured at various positions downwind.

The EEC experiments, Heinrich and Scherwinski [35], Nielsen and Jensen [36], were large scale, continuous two-phase propane releases on flat ground with and without obstacles. They were performed by TüV and Riso in Lathen (Germany, 1989) and were sponsored by the European Commission in the framework of the BA project. This experimental data set is particularly attractive because obstacles were removed during the experiments, allowing a comparison with the unobstructed case, under the same meteorological conditions. During trial EEC-55, which was selected for simulations, ground concentrations were measured at various positions upwind and downwind the fence. Concentration and temperature profiles were also measured at two masts one upwind and one downwind the fence.

The Desert Tortoise experiments [37] were large scale, continuous two-phase ammonia releases on flat ground without obstacles. The experiments were performed by the Lawrence Livermore National Laboratory in Nevada (USA) and were sponsored by the US Coast Guard and Fertilizer Institute. Trial 4 was selected for simulation. During the experiments volume concentration time series were measured at 100 and 800 m downwind from the source and crosswind distances up to 200 m.

The DAT-638 wind tunnel experiment[38] was an instantaneous isothermal SF6 release on inclined ground, performed by the University of Hamburg in the framework of the BA project. Volume concentration time histories were measured at distances 0.613, 1.226 and 1.839 m from the source.

Table 1
Summary of experimental releases

Experiment	Release substance	Release conditions	Meteorological conditions	Terrain and obstacles	Release Ri[a]
Thorney Island 8	Freon 12/nitrogen mixture	Large scale instantaneous isothermal, volume 2000 m^3, relative density 1.63	Wind speed 2.4 m s^{-1} at 10 m, stability D, roughness 0.005 m	Flat	13.9
Thorney Island 21	Freon 12/nitrogen mixture	Large scale instantaneous isothermal, volume 2000 m^3, relative density 2.02	Wind speed 3.9 m s^{-1} at 10 m, stability D, roughness 0.005 m	Flat, semicircular fence 5 m height, 50 m from source	8.6
DAT-638	SF_6	Wind tunnel instantaneous isothermal, volume 450 cm^3, relative density 5.11	Stagnant, roughness 0.0001 m	Flat inclined terrain 11.6%	∞
EEC-55	Propane	Large scale continuous two-phase, mass flow rate 3 kg s^{-1} for 360 s, void fraction 0.61	Wind speed 2.9 m s^{-1} at 10 m, stability D, roughness 0.006 m	Flat terrain, straight thin fence 2 m height, 50 m from source	3.4
Desert Tortoise 4	Ammonia	Large scale continuous two-phase, mass flow rate 108 kg s^{-1} for 381 s	Wind speed 4.5 m s^{-1} at 2 m, stability D, roughness 0.003 m		13.0

[a] Richardson number is defined by $Ri_i = (g(\rho/\rho_a - 1)H)/U_a^2$, for instantaneous releases $Ri_c = (g(\rho/\rho_a - 1))/U_a^2(\dot{m}/\rho U d)$, for continuous releases.

From the above data sets only the experimental data for the sensors closest to the ground were used in the evaluation procedure.

5.2. Evaluation methodology

Quantitative validation of the present model was performed using statistical performance measures. For an evaluation of various performance measures as applied to dense gas dispersion models (see [39]).

The measures used in the present work are following, where the brackets denote arithmetic mean values over all sensors.

5.2.1. FB and NMSE

The fractional bias (FB) and normalized mean square error (NMSE) are defined by

$$\mathrm{FB} \equiv 2\frac{\langle C_\mathrm{p}\rangle - \langle C_\mathrm{o}\rangle}{\langle C_\mathrm{p}\rangle + \langle C_\mathrm{o}\rangle}, \qquad \mathrm{NMSE} \equiv \frac{\langle (C_\mathrm{p} - C_\mathrm{o})^2\rangle}{\langle C_\mathrm{o}\rangle\langle C_\mathrm{p}\rangle} \tag{5.1}$$

where C is the mean concentration for continuous releases (the dose was used, in case of instantaneous releases). Subscripts (p) and (o) denote predicted and observed values, respectively.

The optimum values of FB and NMSE are zero. A positive FB shows that the model predicts values higher than the experimental. Since the absolute values appear in FB, this is affected more by the high values (concentrations close to the centerline and source) than by the low ones.

5.2.2. MRB and MRSE

The mean relative bias (MRB) and the mean relative square error (MRSE) are defined by

$$\mathrm{MRB} \equiv 2\left\langle \frac{C_\mathrm{p} - C_\mathrm{o}}{C_\mathrm{p} + C_\mathrm{o}} \right\rangle, \qquad \mathrm{MRSE} \equiv 4\left\langle \left(\frac{C_\mathrm{p} - C_\mathrm{o}}{C_\mathrm{p} + C_\mathrm{o}}\right)^2 \right\rangle \tag{5.2}$$

The optimum values of MRB and MRSE are zero. A positive MRB shows that the model predicts values higher than the experimental. MRB is more balanced with respect to the high and low concentration values than FB.

5.2.3. MG and VG

The geometric mean (MG) and geometric mean variance (VG) are defined by

$$\mathrm{MG} \equiv \exp\left[\left\langle \ln\frac{C_\mathrm{p}}{C_\mathrm{o}} \right\rangle\right], \qquad \ln(\mathrm{VG}) \equiv \left\langle \left(\ln\frac{C_\mathrm{p}}{C_\mathrm{o}}\right)^2 \right\rangle \tag{5.3}$$

The ideal values are 1 and 0, respectively.

5.2.4. Factor of x

The factor of x is defined as the number of values for which $1/x < C_\mathrm{p}/C_\mathrm{o} < x$.

Table 2
Statistical results of the DISPLAY-2 validation

Measure[a]	Thorney Island 8	Thorney Island 21	DAT-638	EEC-550	EEC-551	Desert Tortoise 4
FB	−0.28	−0.4	−0.56	−0.09	−0.06	0.59
NMSE	0.93	0.65	0.39	0.41	0.51	1.0
MRB	−0.24	−0.49	−0.56	−0.19	−0.25	0.47
MRSE	0.73	0.72	0.35	0.5	0.6	1.7
MG	0.35	0.47	0.56	0.86	0.77	3.0
ln(VG)	15.4	2.1	0.38	0.93	1.4	6.7
FAC2	58.8	78.6	62.5	75	76.5	40
FAC5	88.2	78.6	100	93.8	88.2	60
FAC10	94.1	85.7	100	93.8	88.2	70

[a] Statistical measure variable is dose for the instantaneous and average concentration for the continuous releases.

6. Results and discussion

For the Thorney Island 8 instantaneous, unobstructed release on flat ground the model results in comparison to the experiment are given in Table 2 and Figs. 4–7. In general it can be observed that the model shows relatively good agreement compared to experiment, given the large variability in the experimental results, due to the statistical nature of the atmospheric dispersion process [5]. To take into account the variability of the experimental results one

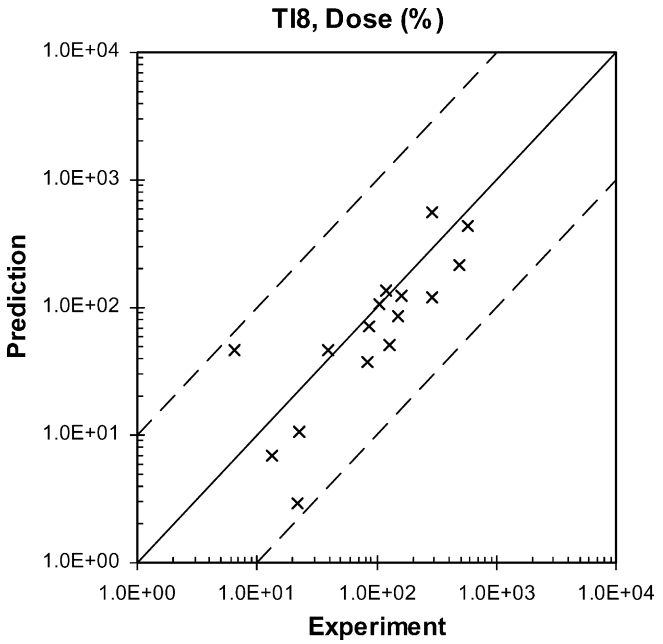

Fig. 4. Experiment Thorney Island 8. Scatter graph of predicted vs. observed dose (%).

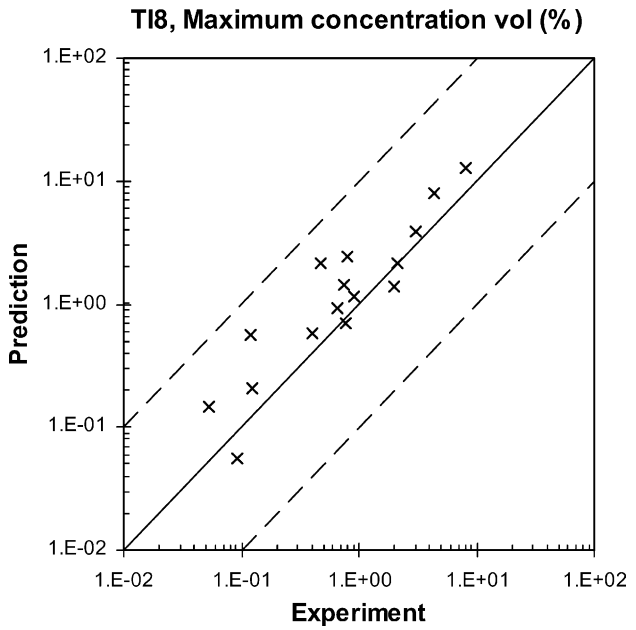

Fig. 5. Experiment Thorney Island 8. Scatter graph of predicted vs. observed maximum concentration (vol.%).

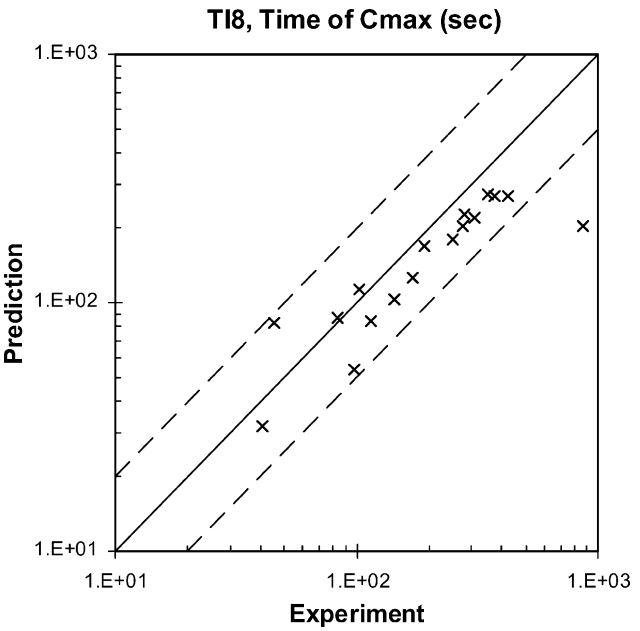

Fig. 6. Experiment Thorney Island 8. Scatter graph of predicted vs. observed arrival time (s) to the maximum concentration.

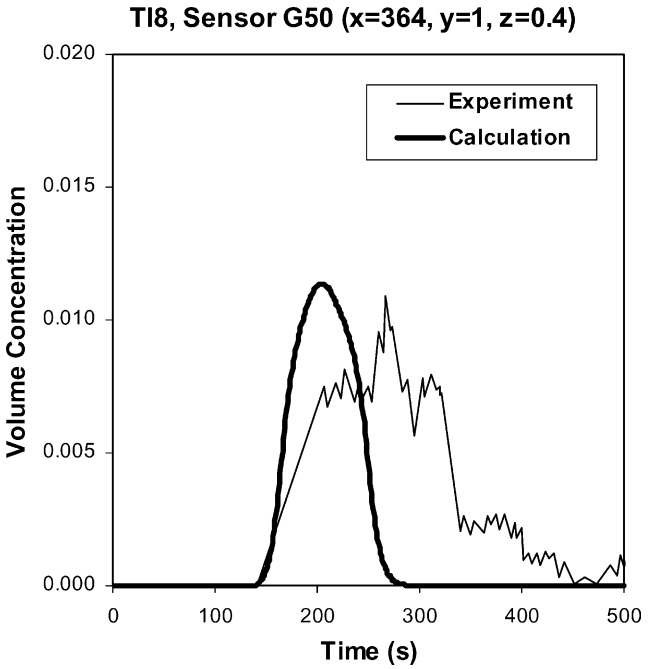

Fig. 7. Experiment Thorney Island 8. Predicted vs. observed concentration time history for sensor at position (364, 1, 0.4).

should compare their model with repeats under the same experimental conditions, as has been done for the Warren Spring Data from the BA project by Sweatman and Chatwin [40], but this was not possible with the present experimental data sets.

The statistical measures in Table 2 and the scatter plot in Fig. 4 show that the model underestimates the dose and that 88% of the predicted dose points lie within a factor of 5 from the experiment. Figs. 5 and 6 present scatter plots of predicted versus observed maximum concentration and time of maximum concentration. The tendency is for the model to overestimate the maximum concentration approximately by a maximum factor of 5 and underestimate the time at which this occurs approximately by a maximum factor of 2. Fig. 7 shows the predicted concentration time history on the cloud centerline, 364 m downwind the source initial position.

The above model behavior is consistent with a model cloud traveling faster than in the experiment, since a faster moving cloud will exhibit lower arrival times, lower residence times leading to lower dose and lower time to dilute, leading to higher concentrations.

The faster moving cloud (at least during the initial phases of dispersion) can be observed in Fig. 8, where the predicted cloud footprint area versus time is compared against a mean line drawn through the experimental data, which were determined by photographs [41]. During the initial period from 0 to 5 s the experimental observations showed a very small area increase, which indicates a hesitation of the cloud to start its gravity slumping phase, possibly due to complicated three-dimensional flow structure and associated high turbulence

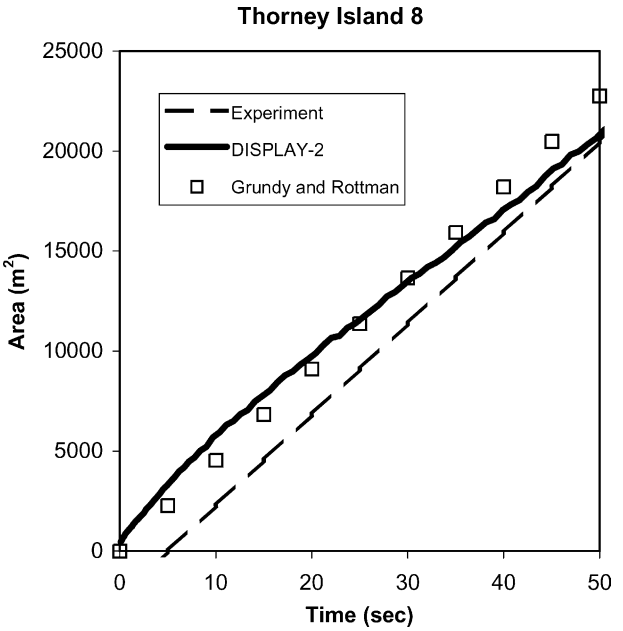

Fig. 8. Experiment Thorney Island 8. Predicted footprint area change with time vs. mean curve through experimental observations [39] and theory [31].

levels. Also shown in this figure is the linear dependence suggested by Grundy and Rottman [32], whose gradient is observed to be very close to the mean experimental.

It can be observed from Fig. 8 that the present model cannot reproduce this initial phase. In general it overestimates the cloud area, but the deviations from the experimental linear dependence are acceptably small. A discussion on the factors responsible for the behavior of the present model is following.

The present model does not account for the three-dimensional structure of the initial flow and turbulence field around the cylinder at time zero, i.e. before removing the containment. It is expected that the initial turbulence levels around the cylinder would be high, due to high shear, especially downwind the cylinder. Such high turbulence levels would lead to increased entrainment during this initial phase. The present entrainment model does not account for any such additional initial phase effects. Additionally one could also argue on the sudden turbulence increase and its effect on entrainment, due to the shear generated by the initial fast removal of the cylinder containment. This effect though is expected to be small.

Another factor affecting the present model results is the hydrostatic assumption. The pressure forces from the ambient air to the cloud are neglected. This leads to an initially accelerating cloud. The present model though accounts for the frictional forces from the ambient air at the cloud top and thus limits the cloud footprint area increase to acceptable levels. The most realistic and desirable modeling approach would be to combine both frictional and pressure forces from the ambient air in one model.

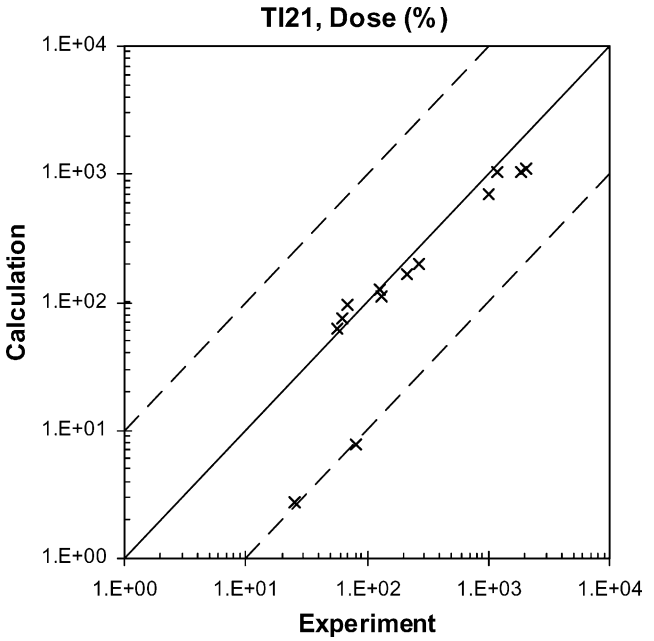

Fig. 9. Experiment Thorney Island 21. Scatter graph of predicted vs. observed dose (%).

The model predictions compared against the experimental concentrations of the Thorney Island 21 trial are shown in Table 2 and Figs. 9–12. In general it can be observed that the results are in good agreement with the experiment. More specifically, the model underestimates the dose and nearly 80% of the predicted dose points lie within a factor of 2 from the experiment. The model also overestimates the maximum concentration approximately by factor of 5 and underestimates the arrival times, approximately by factor of 2. It can also be observed that the general trend is similar to the unobstructed trial 8, i.e. underestimation of the dose, overestimation of the maximum concentration and underestimation of the arrival times, a trend which can similarly be attributed to the factors mentioned above in the Thorney Island 8 discussion, but also to the fact that the present model does not account for the three-dimensional structure of the flow field around the semicircular fence obstacle.

In order to assess the importance of the factors affecting the modeling of the obstacle we have plotted in Fig. 12, which corresponds to the first sensor on the centerline downwind the obstacle, results from two extra calculations, one without any obstacle at all and one accounting only for the obstacle drag, i.e. neglecting the extra obstacle entrainment. Comparing to the full model curve (thick solid line) it can be observed that both obstacle effects contribute but that the most important is the extra entrainment effect.

Similar comparisons were performed for sensors far from the obstacle. It was found that the higher the distances of the sensors from the obstacle the lower is the deviation between the model results with and without obstacle effects. This behavior was expected, because as the distance from the obstacle increases, the total entrained ambient air becomes much bigger than any local entrainment enhancement at the downwind side of the obstacle.

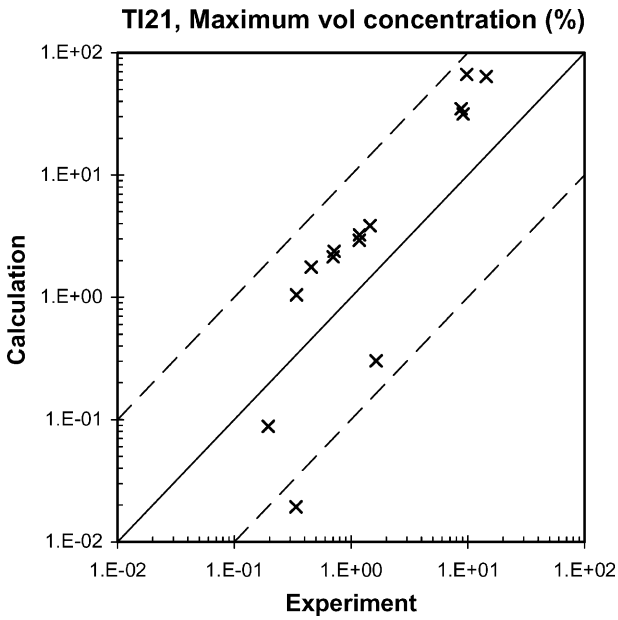

Fig. 10. Experiment Thorney Island 21. Scatter graph of predicted vs. observed maximum concentration (vol.%).

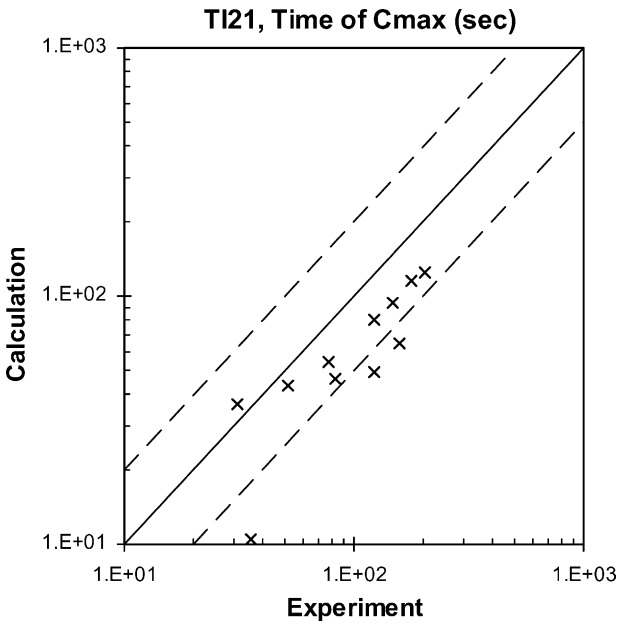

Fig. 11. Experiment Thorney Island 21. Scatter graph of predicted vs. observed arrival time (s) to the maximum concentration.

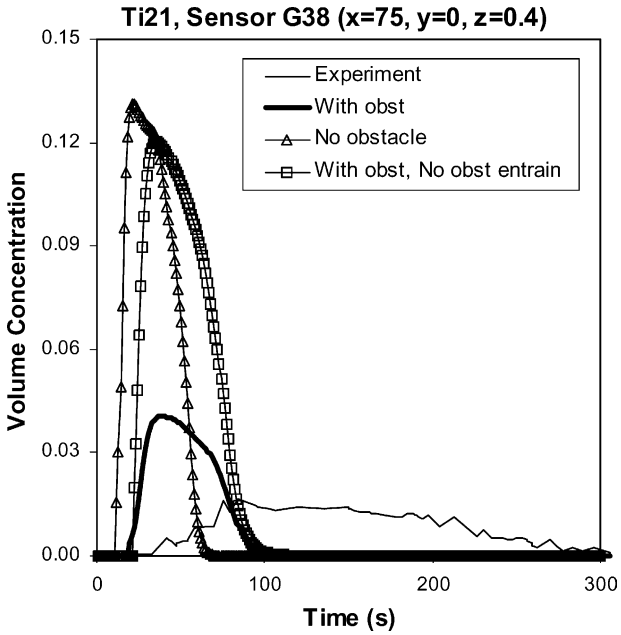

Fig. 12. Experiment Thorney Island 21. Predicted vs. observed concentration time history for sensor at position (75, 0, 0.4).

The two previous validation cases were for large scale releases on flat ground. The model results for the DAT-638 experiment, which is a wind tunnel experiment on inclined ground, are shown in Table 2 and Figs. 13–16. The calculations have been performed in large scale. Geometrical conversion from small to large scale was performed using a length scale factor of 164.5. This value sets the closest large scale sensor at 100 m from the initial source position. Similarity between large and small scale was preserved by multiplying the wind tunnel time by a factor of $164.5^{1/2} = 12.83$, since length and time scales for instantaneous releases are connected, following König [42]:

$$L_{\mathrm{ci}} = V_0^{1/3}, \qquad T_{\mathrm{ci}} = \left(\frac{L_{\mathrm{ci}}}{g'}\right)^{1/2}, \qquad g' = \frac{g(\rho_0 - \rho_{\mathrm{air}})}{\rho_{\mathrm{air}}} \tag{6.1}$$

where V_0 is the initial volume of the release, $g = 9.81\,\mathrm{m^2\,s^{-1}}$ and ρ_0 is the initial dense gas density.

Figs. 13 and 14 show the comparison between predicted and measured concentration time histories, 100 m down hill from the initial source position, at the symmetry plane ($y = 0$) and 75 m laterally from it. It can be observed that there is a good agreement with the experiment, as far as arrival times and maximum concentrations are concerned, but there is a tendency for the model to under predict the cloud residence times and eventually the dose. Figs. 15 and 16 show a similar comparison 300 m down hill at the symmetry plane and 63 m laterally from it. At this distance the model underestimates the concentrations but

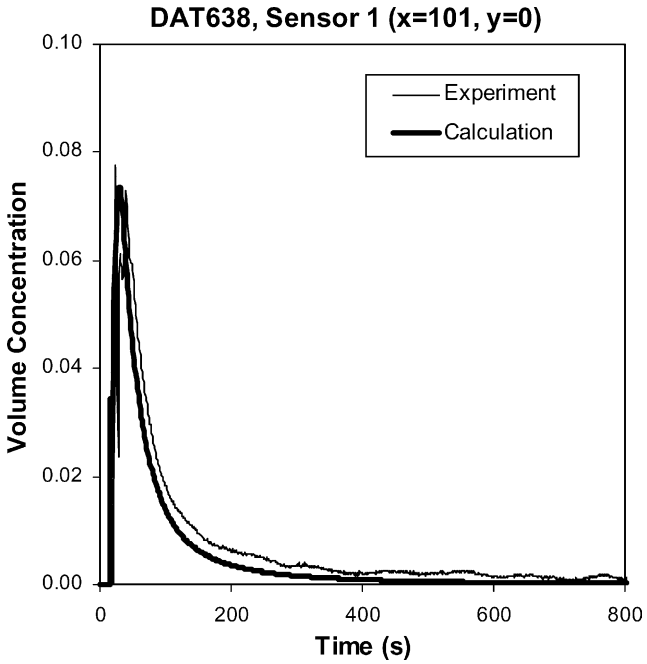

Fig. 13. Experiment DAT-638. Predicted vs. observed concentration time history for sensor at position (101, 0).

still predicts very well the arrival times. The validation statistics are shown in Table 2. It can be observed that the model underestimates the dose by factor of 2 for 62.5% of the points and factor of 5 for all points.

The previous validation cases were for isothermal and instantaneous releases. We shall examine next the model behavior for continuous two-phase releases. The model results for the EEC-55 propane experiment are shown in Figs. 17–19 and Table 2. Fig. 19 shows a comparison between predictions and experiment for sensor No. 38 at position (63, 3, 0.05), i.e. close to the jet symmetry axis and 10 m downwind the obstacle. The time period from 0 to 185 s corresponds to the obstructed case. The fence was removed at 185 s. The release ended at 360 s. It can be observed that the model (thick solid line) predicts well the average concentration in the obstructed case and slightly underestimates it in the unobstructed. In order to assess the obstacle modeling we have plotted in the same figure the model predictions without any obstacle and the predictions with only the obstacle resistance terms, i.e. without the obstacle's extra entrainment. Similarly to the Thorney Island 21 case examined before, it can be observed that both obstacle resistance and extra entrainment effects contribute, but that the dominant is the second.

The present calculations were performed assuming a void fraction of 0.61. In order to assess the effect of the rainout model, we have also plotted in Fig. 19 the prediction without rainout. It can be observed that this effect is small in this case. A similar small effect was also observed for the other sensors considered.

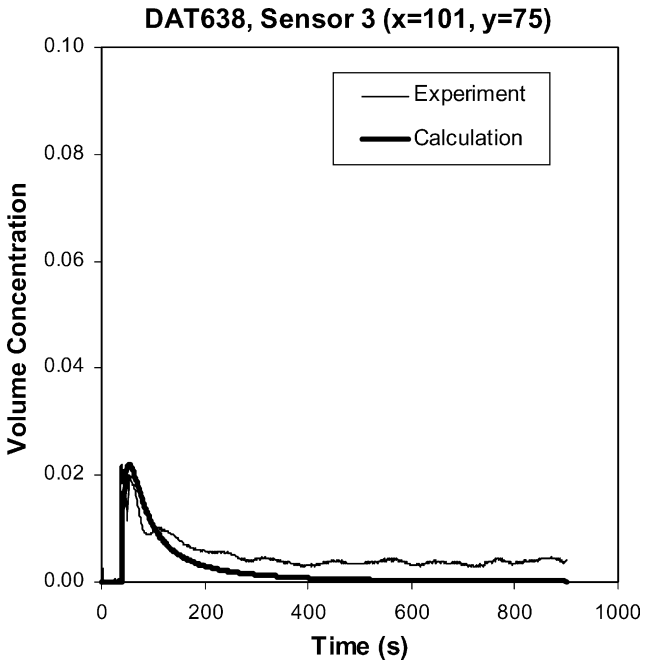

Fig. 14. Experiment DAT-638. Predicted vs. observed concentration time history for sensor at position (101, 75).

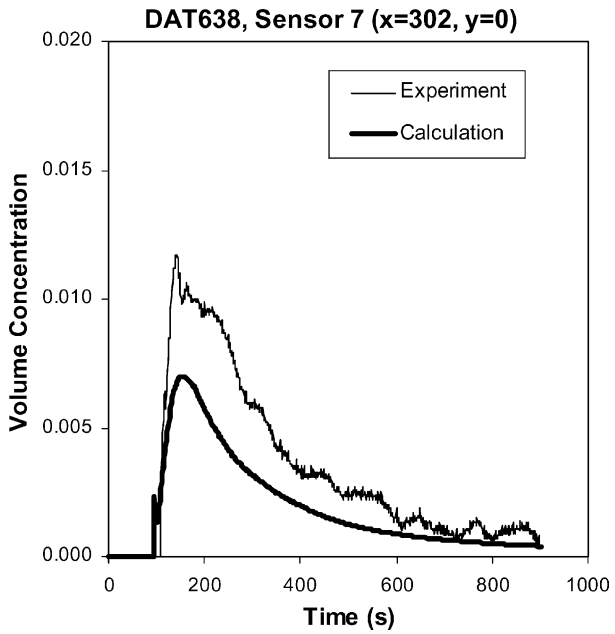

Fig. 15. Experiment DAT-638. Predicted vs. observed concentration time history for sensor at position (302, 0).

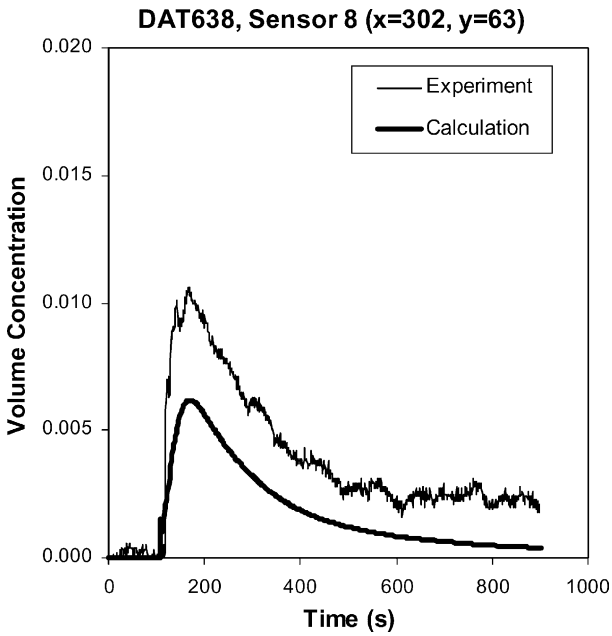

Fig. 16. Experiment DAT-638. Predicted vs. observed concentration time history for sensor at position (302, 63).

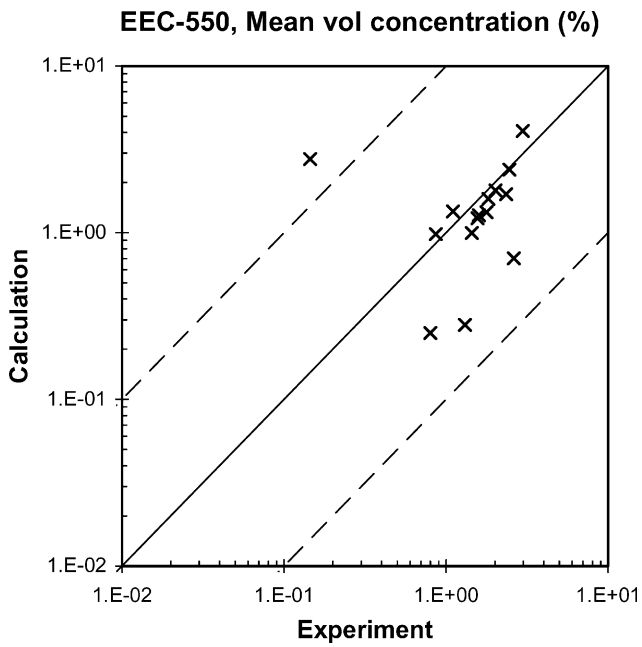

Fig. 17. Experiment EEC-550. Scatter graph of predicted vs. observed average concentration (vol.%).

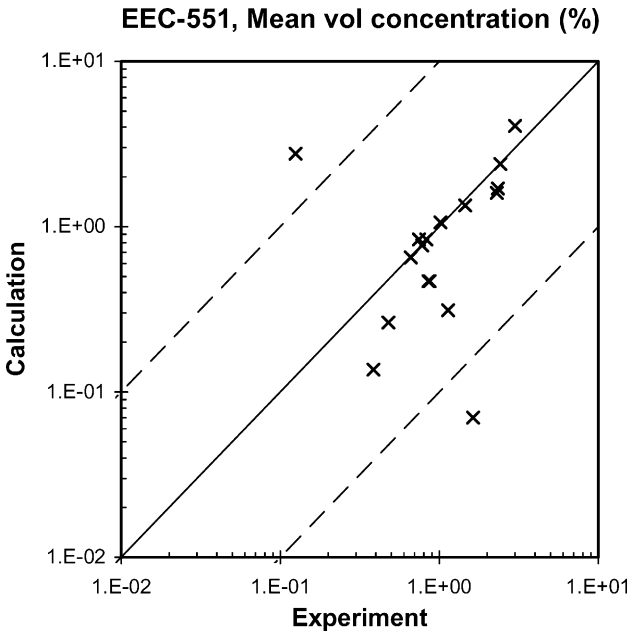

Fig. 18. Experiment EEC-551. Scatter graph of predicted vs. observed average concentration (vol.%).

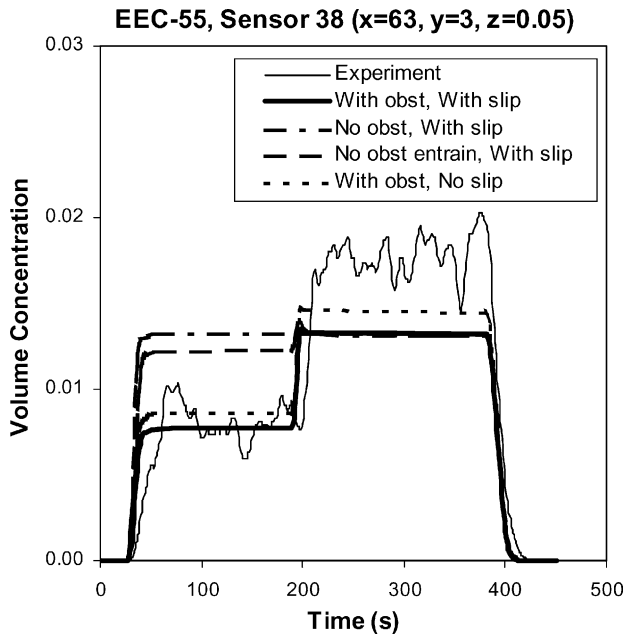

Fig. 19. Experiment EEC-55. Predicted vs. observed concentration time history for sensor at position (63, 3, 0.05).

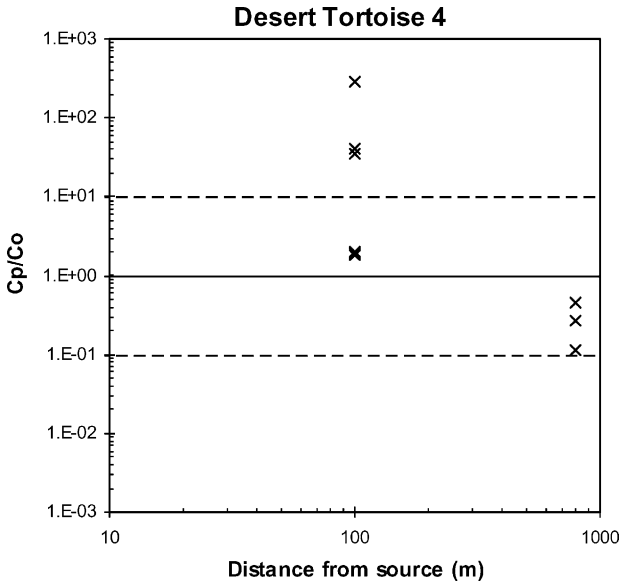

Fig. 20. Experiment Desert Tortoise 4. Ratio of predicted vs. observed average concentration as function of distance from source.

In Table 2 the unobstructed case EEC-550 is examined separately from the obstructed one EEC-551. For both these cases it can be observed that the model under predicts the average concentrations and that 75% of the concentration points lie within factor of 2 from the experiment.

Figs. 20 and 21 show the model predictions in comparison to the Desert Tortoise trial 4 ammonia experiment. Fig. 20 shows the ratio of predicted to observed average concentrations for the sensors closest to the ground (1 m distance from it) as function of distance from source. From this figure and also from Table 2, it can be observed that 70% of the considered concentration points lie within a factor of 10 from the experimental. It can also be observed that there is a trend in the model to overestimate the concentrations at 100 m and underestimate them at a distance of 800 m from the source. The point with the maximum overestimation at 100 m corresponds to a crosswind distance of 30 m from the cloud axis. The high overestimation at this location is due to experimental cloud meandering, which can be confirmed by considering the crosswind symmetric sensor, for which the overestimation is only by a factor of 2. The next two higher overestimation points at the same axial distance from the source correspond to a lateral distance of 45 m. This overestimation shows that the model over predicts the cloud lateral spreading at relatively small distances from the source, a fact, which can explain the underestimation mentioned earlier at high distances. The increased lateral spreading at low distances from source can be attributed to an overestimation of the liquid phase, possibly due to the rainout model used. Fig. 21 compares the concentration time histories on the plume centerline, 100 m from the source and 1 m from ground. Included in this figure is the prediction without rainout. It can be observed that there is a good prediction of arrival times in both cases. It can also be observed

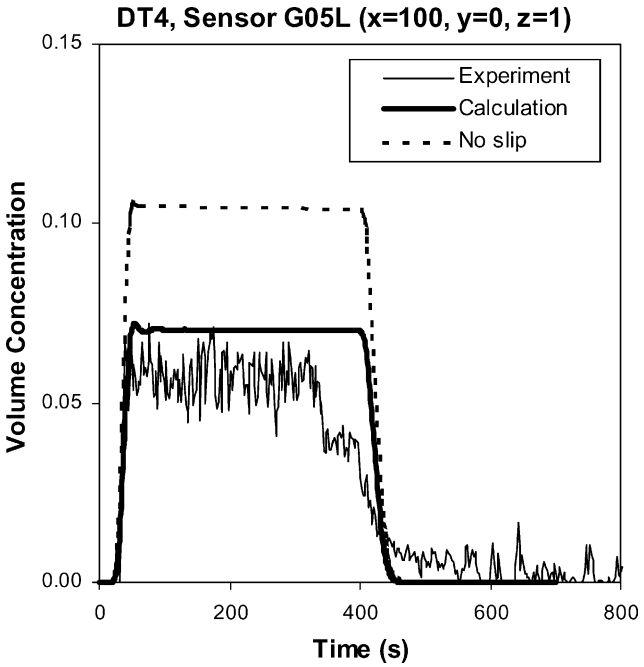

Fig. 21. Experiment Desert Tortoise 4. Predicted vs. observed concentration time history for sensor at position (100, 0, 1).

that the modeling of the rainout effect is very important in this case, in comparison to the EEC-55 experiment, due both to the much higher release rate and to the higher latent heat for evaporation of ammonia ($1.4 \times 10^6\,\mathrm{J\,kg^{-1}}$), with respect to propane (4.2×10^5).

7. Conclusions and future work

In the present contribution the two-dimensional shallow layer model DISPLAY-2 has been presented in detail.

The model performance has been evaluated against theoretical results and a wide range of experimental conditions. In general the model predictions were found to be in reasonably good agreement with theory and experiments. More specifically the following conclusions can be drawn.

The deviations of the model predictions from the theoretical gravity spreading rates for constant volume [32] and constant flux [33] gravity currents were found to be relatively small, if one models turbulent friction at the top of the cloud, without any Richardson dependence.

For the Thorney Island 8 and 21 [34], large scale instantaneous releases on flat ground, the model was found to underestimate the dose by factor of 5, overestimate the maximum concentrations by factor of 5 and underestimate the arrival times by a factor of 2.

For the Hamburg DAT-638 instantaneous wind tunnel release on 11.6% slope [38], the model was found to predict arrival times well both at low and high distances from source, to predict the maximum concentrations well close to source and underestimate them at higher distances and in general predict lower residence times than experimental. Additionally the model was found to underestimates the dose by factor of 2 for 62.5% of the points and factor of 5 for all points.

For the EEC-55 propane experiment with and without fence on flat ground [35,36], it was found that the model in general under predicts the average concentrations and that 75% of the concentration points lie within factor of 2 from the experiment.

For the Desert Tortoise 4 ammonia experiment on flat ground [37], it was found that the model overestimates the concentrations close to the source and underestimates them far away. In general it was found that 70% of the concentration points lie within a factor of 10 from the experimental.

Regarding the proposed modeling of the obstacles it was shown, based on the Thorney Island 21 and the EEC-55 experiment, that the present method is able to give predictions in agreement with experimental behavior and it was found that both the drag exerted by the obstacle to the cloud and the extra vorticity generated when the cloud passes over the obstacle play a role and that the most important effect is the second.

Regarding the proposed modeling of rainout in case of two-phase releases it was found based on the EEC-55 and Desert Tortoise 4 experiments, that predictions with the present formulation can be significantly improved with respect to the case where rainout is entirely neglected.

For the future, the present model should be evaluated in a wider range of conditions and in particular against experiments where repeats under the same experimental conditions are available, in order to account of the experimental variability. Additionally the model performance, when using non top hat profiles should be evaluated. Finally, the modeling of obstacle effects in shallow layer modeling should be further investigated and extended to account for more complicated situations, using help from CFD.

Acknowledgements

The authors would like to thank the European Commission for the funding of this work under the Human Capital and Mobility Program. The first author would like to give special thanks to all of his co-authors for their patience and substantial support. Additionally I would like to thank the reviewers of this paper for their very important comments, but also Dr. Ivan Kovalets, Euratom grant holder in NCSR Demokritos, for the very fruitful discussions we had on the subject of dense gas dispersion modeling.

Appendix A

For one falling droplet, in the laminar flow regime, the droplet velocity is proportional to the square of its diameter $w_0 D^2$ [29].

The mean droplet fall velocity is obtained as the ratio of the vertical liquid flux over the liquid mass per unit volume.

Assuming that droplets are distributed in diameter according to the Marshall and Palmer distribution, the vertical liquid flux becomes

$$\rho q_l w_{ld} = \int_0^\infty (n_0 e^{-\lambda D}) \left(\frac{\pi}{6}\rho_l D^3\right) (w_0 D^2)\, dD$$

while the liquid mass per unit volume

$$\rho q_l = \int_0^\infty (n_0 e^{-\lambda D}) \left(\frac{\pi}{6}\rho_l D^3\right) dD$$

It can be shown that the above integrals take the form

$$\rho q_l w_{ld} = \frac{n_0 \pi \rho_l}{6} w_0 \frac{\Gamma(5)}{\lambda^6} = 0.4 \frac{n_0 \pi \rho_l}{\lambda^6} w_0$$

and

$$\rho q_l = \frac{n_0 \pi \rho_l}{6} \frac{\Gamma(4)}{\lambda^4} = \frac{n_0 \pi \rho_l}{\lambda^4}$$

Combining the previous relations, it can be shown that

$$w_{ld} = \frac{\rho q_l w_{ld}}{\rho q_l} = \frac{0.4 w_0}{(n_0 \pi)^{0.5}} \left(\frac{\rho q_l}{\rho_l}\right)^{1/2}$$

References

[1] S. Andronopoulos, J.G. Bartzis, J. Würtz, D. Asimakopoulos, Modeling the effects of obstacles on the dispersion of denser than air gases, J. Hazard. Mater. 37 (1994) 327–352.

[2] J.C. Statharas, J.G. Bartzis, A.G. Venetsanos, J. Würtz, Prediction of ammonia releases using the ADREA-HF code, Process Safety Prog. 12 (1993) 118–122.

[3] N.J. Duijm, B. Carissimo, A. Mercer, C. Bartholome, H. Giesbrecht, Development and test of an evaluation protocol for heavy gas dispersion models, J. Hazard. Mater. 56 (1997) 273–285.

[4] J. Würtz, J.G. Bartzis, A.G. Venetsanos, S. Andronopoulos, J. Statharas, R. Nijsing, A dense vapour dispersion code package for applications in the chemical and process industry, J. Hazard. Mater. 46 (1996) 273–284.

[5] J. Würtz, A transient one-dimensional shallow layer model for dispersion of denser-than-air gases in obstructed terrains under non-isothermal conditions, Report EUR 15343 (EN), 1993.

[6] R.N. Meroney, Transient characteristics of dense gas dispersion. I. A depth-averaged numerical model, J. Hazard. Mater. 9 (1984) 139–157.

[7] S. Ott, M. Nielsen, Shallow layer modeling of dense gas clouds, Risoe National Laboratory, Roskilde, Denmark, Risoe-R-901 (EN), November 1996.

[8] R.K.S. Hankin, R.E. Britter, TWODEE: the Health and Safety Laboratory's shallow layer model for heavy gas dispersion. 1. Mathematical basis and physical assumptions, J. Hazard. Mater. A 66 (1999) 211–226.

[9] R.K.S. Hankin, R.E. Britter, TWODEE: the Health and Safety Laboratory's shallow layer model for heavy gas dispersion. 2. Outline and validation of the computational scheme, J. Hazard. Mater. A 66 (1999) 227–237.

[10] R.K.S. Hankin, R.E. Britter, TWODEE: the Health and Safety Laboratory's shallow layer model for heavy gas dispersion. 3. Experimental validation (Thorney Island), J. Hazard. Mater. A 66 (1999) 239–261.

[11] D.M. Webber, S.J. Jones, D. Martin, A model for the motion of a heavy gas cloud released on a uniform slope, J. Hazard. Mater. 33 (1993) 101–122.

[12] R.E. Britter, J.E. Simpson, Experiments on the dynamics of a gravity current head, J. Fluid Mech. 88 (1978) 223–240.

[13] C. Housiadas, G.T. Amanatidis, J.G. Bartzis, Prediction of orographic precipitation using Cartesian co-ordinates and a singles prognostic equation for the water substance, Boundary Layer Meteorol. 56 (1991) 245–260.
[14] R.A. Pielke, Mesoscale Meteorological Modeling, Academic Press, New York, 1984, 612 pp.
[15] A.G. Venetsanos, S. Andronopoulos, J. Statharas, J.G. Bartzis, Local scale dispersion model evaluation exercise, in: Proceedings of the Sixth International Conference on Air Pollution 98, Genoa, Italy, 28–30 September 1998.
[16] R.J. Carpenter, R.P. Cleaver, P.J. Waite, M.A. English, The calibration of a simple model for dense gas dispersion using the Thorney Island, phase I data, J. Hazard. Mater. 16 (1987) 293–313.
[17] C.J. Wheatley, A.J. Prince, Translational cloud speeds in the Thorney Island trials: mathematical modeling and data analysis, J. Hazard. Mater. 16 (1987) 185–199.
[18] D.M. Webber, P.W.M. Brighton, Inviscid similarity solutions for slumping from a cylindrical tank, Trans. ASME 108 (1986) 238–240.
[19] K.J. Eidsvik, A model for heavy gas dispersion in the atmosphere, Atmos. Environ. 14 (1980) 769–777.
[20] H. Tennekes, J.L. Lumley, A First Course in Turbulence, MIT Press, Cambridge, MA, 1972.
[21] H. Kato, O.M. Philips, On the penetration of a turbulent layer into a stratified fluid, J. Fluid Mech. 37 (1969) 643–655.
[22] D. Stretch, The dispersion of slightly dense contaminants in a turbulent boundary layer, University of Cambridge, 1986.
[23] M. Nielsen, Dense gas dispersion in the atmosphere, Risoe National Laboratory, Roskilde, Denmark, Risoe-R-1030 (EN), September 1998.
[24] O.G. Sutton, Micrometeorology, McGraw-Hill, New York, 1953, p. 281.
[25] D.D. Papailiou, P.S. Lykoudis, Turbulent vortex streets and the entrainment mechanism of the turbulent wake, J. Fluid Mech. 62 (1974) 11–31.
[26] R.P. Cleaver, M.G. Cooper, A.R. Halford, Further development of a model for dense gas dispersion over real terrain, J. Hazard. Mater. 40 (1995) 85–108.
[27] I.E. Idelchik, Handbook of Hydraulic Resistance, second ed., Hemisphere, Washington, DC, 1986, p. 170.
[28] Y. Ogura, T. Takahashi, Numerical simulation of the life cycle of a thunderstorm cell, Monthly Weather Rev. 99 (1971) 895–911.
[29] R.R. Rogers, A Short Course in Cloud Physics, Pergamon Press, Oxford, 1979.
[30] S.V. Patankar, Numerical Heat Transfer and Fluid Flow, Hemisphere, Washington, DC, 1980.
[31] Ch. Hirsch, Numerical computation of internal and external flows, in: Computational Methods for Inviscid and Viscous Flows, vol. 2, Wiley, Chichester, 1990.
[32] R.E. Grundy, J.W. Rottman, The approach to self similarity of the solutions of the shallow water equations representing gravity current releases, J. Fluid Mech. 56 (1985) 39–53.
[33] R.E. Britter, The spread of a negatively buoyant plume in a calm environment, Atmos. Environ. 13 (1979) 1241–1247.
[34] J. McQuaid, B. Roebuck, Large scale field trials on dense vapour dispersion, Report EUR 10029 (EN), 1985.
[35] M. Heinrich, R. Scherwinski, Research on propane releases under realistic conditions—determination of gas concentrations considering obstacles, Tüv Final Project Report, December 1990.
[36] M. Nielsen, N.O. Jensen, Continuous release dense gas field experiments with obstacles, Final Report on Project BA.X2, Riso National Laboratory, Riso-M-2923, 1991.
[37] H.C. Goldwire Jr., Desert Tortoise series data report: 1983 pressurized ammonia spills, UCID-20562, Laurence Livermore National Laboratory, Livermore, CA, 1985.
[38] K. Marotzke, Wind tunnel modelling of density current interaction on an inclined plane, Paper presented at the CEC project BA meeting, Meteorological Institute of Hamburg University, Lathen, 1989.
[39] N.J. Duijm, S. Ott, M. Nielsen, An evaluation of validation procedures and test parameters for dense gas dispersion models, J. Loss Prevention Process Ind. 9 (5) (1996) 323–338.
[40] W.L. Sweatman, P.C. Chatwin, Dosages from instantaneous releases of dense gases in wind tunnels and into a neutrally stable atmosphere, Boundary Layer Meteorol. 77 (1996) 211–231.
[41] P.W.M. Brighton, A.J. Prince, D.M. Webber, Determination of cloud area and path from visual and concentration records, J. Hazard. Mater. 11 (1985) 155–178.
[42] G. König, Windkanalmodellierung der Ausbreitung störfallartig freigesetzer Gase schwerer als Luft, Hamburg University, Hamburger Geophysikalische Einzelschriften, Reihe A, Wissenschaftliche Abhandlungen, GML Wittenborn Sohne, Heft 85, 1987.